Study on gas-liquid two-phase flow law considering gas dissolution during gas invasion in gas field drilling

Haikang He, *Baojiang* Sun*, *Xiaohui* Sun, *Zhiyuan* Wang, and *Xuefeng* Li

China University of Petroleum (East China), Qingdao, Shandong, China.

Abstract. During the drilling and development of sour natural gas (including CO_2 and H_2S) fields, due to the high solubility of sour natural gas in drilling fluid, the concealment after gas invasion increases, resulting in well control accidents. Therefore, it is of great significance for gas field development to deeply study and understand the solubility of acid gas and the flow law of annular air and liquid after the gas invasion. In this paper, a multiphase flow equation considering gas dissolution is established. Based on the existing solubility experimental data, the equation of state for predicting the solubility of sour natural gas is optimized. It is found that the fugacity activity method using Peng and Robinson equation of state has the highest accuracy. The analysis of gas-liquid two-phase law through a specific example shows that considering the influence of gas dissolution, the increment of mud pit changes slowly and the concealment of gas invasion is strong. When the content of acid gas in drilling fluid is higher, the time for the pit gain change monitored on the ground increases and the concealment further increases, which is more harmful to the safety control of wellbore pressure.

1 Introduction

The rapid development of economy has increased the demand for energy. It is necessary to increase the drilling of natural gas fields, mainly those containing H_2S and CO_2 acid gas. Such gas fields are concentrated in Sichuan and Chongqing, China, with CO_2 content of 8.5% ~ 9.6% and H_2S content of 15.6% ~ 24.1%, belonging to typical high acid oil and gas fields [1,2]. Gas invasion is frequently encountered in the acid gas field drilling process [3, 4]. The intrusive gas quickly dissolves into drilling fluid or intrusive formation water under high pressure, which is difficult to monitor and find, resulting in blowout accidents. Therefore, it is of great significance to optimize the high-precision calculation model of acid gas solubility and analyze the influence of gas solubility on the law of multiphase flow.

Scholars have obtained a large number of experimental data on the solubility of natural gas [5, 6, 7, 8]. At the same time, the corresponding prediction model is established based on phase equilibrium [9, 10], among which the model of Duan [11] was widely used because of its high precision. There are few reports on the solubility of natural gas including CO_2. Zirrahi

* Corresponding author: sunbj1128@126.com

et al. [12] and Ziabakhsh-Ganji [13] established the corresponding prediction model by using the fugacity-activity method. Subsequently, Li [14] compared the phase equilibrium prediction accuracy of fugacity-fugacity model and fugacity-activity model for CO_2-CH_4-H_2S-brine, and found that the fugacity-activity model has higher accuracy, but ignored the impact of the selection of equation of state on the calculation accuracy of the model.

During drilling, the high solubility of formation invasion fluid under high temperature and high pressure leads to the increase of the concealment of gas invasion. Sun et al. [15], Xu et al. [16], Yin et al. [17] considered the influence of gas dissolution in oil-based drilling fluid on the law of multiphase flow, and established the corresponding multiphase flow model. Through the analysis of mud pit increment and gas phase volume fraction, it is found that the high solubility of gas leads to the increase of gas invasion monitoring time. At the same time, the mud pit increment of oil-based drilling fluid has no obvious change of water-based drilling fluid. If the gas solubility is not considered, the bottom hole pressure will be underestimated.

To sum up, although there are a large number of accurate models for gas solubility prediction, the selection of gas equation of state is still a problem that needs further research. At the same time, for the application of gas solubility during drilling gas invasion, the existing models are mainly concentrated in oil-based drilling fluid with greater solubility. The influence of gas dissolution in water-based drilling fluid on the law of multiphase flow in annulus is ignored. Therefore, this paper first establishes a multiphase flow model considering gas dissolution, optimizes the equation of state in gas solubility prediction, and obtains a more accurate applicable state equation. Finally, a specific example is used to analyze the influence of gas solubility on annular multiphase flow.

2 Model establishment

2.1 Establishment of multiphase flow equations

According to the mass conservation theorem, the physical model of continuity equation is established considering the dissolution of gas in drilling fluid. The continuity equation of gas phase is as follows:

Free gas:

$$\frac{\partial}{\partial t}\left(\rho_g E_g A\right)+\frac{\partial}{\partial z}\left(\rho_g E_g A u_g\right)=q_g\text{-}m_{g-L} \tag{1}$$

Dissolved gas:

$$\frac{\partial}{\partial t}\left(\rho_{sg} R_{sm} E_m A\right)+\frac{\partial}{\partial z}\left(\rho_{sg} R_{sm} E_m A u_m\right)=m_{g-L} \tag{2}$$

Where, ρ_g is the free gas density at local temperature and pressure, kg/cm^3; E_g is the free gas volume fraction, dimensionless; u_g is the upward velocity of free gas, m/s; ρ_{sg} is the density of standard gas at local temperature and pressure, kg/cm^3; E_m is the volume fraction of drilling fluid, dimensionless; u_m is the upward velocity of drilling fluid, m/s; R_{sm} is the solubility of gas in drilling fluid, m^3/m^3; q_g is the mass of gas produced per unit time per unit thickness, kg/(s·m). For gas-phase non production interval, q_g in Eq. (1) is equal to 0, regardless of gas production. $m_{g\text{-}L}$ is the mass transfer rate from gas phase to liquid phase, kg/(m·s).

Mass conservation equation of liquid phase:

$$\frac{\partial}{\partial t}(A\rho_m E_m)+\frac{\partial}{\partial z}(A\rho_m E_m u_m)=m_{g-L} \tag{3}$$

where, ρ_m is the drilling fluid density at local temperature and pressure, kg/cm^3.

According to the momentum theorem, all external forces of the physics such as the rate of change of momentum and time possessed by the object, are expressed as:

$$\frac{d}{dt}(mu)=\sum F \tag{4}$$

Momentum change rate in gas phase:

$$F_g=\frac{\partial\left(E_g A\rho_g u_g\right)}{\partial t}+\frac{\partial\left(E_g A\rho_g u_g{}^2\right)}{\partial z}+\frac{\partial\left(R_{sm}\rho_{sg}E_m A u_m\right)}{\partial t}+\frac{\partial\left(R_{sm}\rho_{sg}E_m A u_m{}^2\right)}{\partial z} \tag{5}$$

Momentum change rate in liquid phase:

$$F_m=\frac{\partial\left(A\rho_m u_m E_m\right)}{\partial t}+\frac{\partial\left(A\rho_m u_m{}^2 E_m\right)}{\partial z}-\frac{\partial\left(R_{sm}\rho_{sg}E_m A u_m\right)}{\partial t}-\frac{\partial\left(R_{sm}\rho_{sg}E_m A u_m{}^2\right)}{\partial z} \tag{6}$$

Therefore, the momentum equation of multiphase flow in annulus is:

$$\sum_{i=g,m}F_i=-Ag\cos\alpha(\sum_{i=g,m}^{n}\rho_i E_i)-\frac{d(AP)}{dz}-A\left|\frac{dP}{dz}\right|_{fr} \tag{7}$$

Where, F_g and F_m are the momentum of gas phase and liquid phase, respectively.

2.2 Auxiliary equation

2.2.1 Calculation of frictional pressure drop

(1) Single phase flow

Sun et al.[18] applied the flow of power-law fluid to the liquid phase flow equation:

$$F_r=\frac{2fu_{am}^2\rho_{am}}{D_e} \tag{9}$$

Re<2000

$$f=\frac{8k}{\rho_{am}u_{am}^2}\left[\frac{8u_{am}}{D_e}\frac{3n+1}{4n}\right]^n \tag{10}$$

Re>2000

$$\frac{1}{\sqrt{f}}=\frac{2k}{n^{0.75}}\log\left[\mathrm{Re}\left(\frac{f}{4}\right)^{1-\frac{n}{2}}\right]-\frac{0.2}{n^{1.2}} \tag{11}$$

(2) Gas-liquid two-phase flow

Bubbly flow:

$$F_r = \frac{2fu_{am}^2\rho_{am}}{D_e} \tag{12}$$

Slug flow and churn flow:

$$F_r = \frac{2f\left(1-E_g\right)u_{am}^2\rho_{am}}{D_e} \tag{13}$$

$$\frac{1}{\sqrt{f}} = -4\log\left(\frac{\varepsilon_e}{3.71}D_e - 5.05\log\frac{A}{\mathrm{Re}}\right) \tag{14}$$

$$A = \left(\frac{\varepsilon_e}{2.549D_e}\right)^{1.11} + \left(\frac{7.149}{\mathrm{Re}}\right)^{0.898} \tag{15}$$

Annular fog flow:

$$F_r = \frac{2fu_{am}^2\rho_{am}}{D_eE_g^2} \tag{16}$$

$$f = 0.079\left[1+\frac{75\left(1-E_g\right)}{\mathrm{Re}\,\mathrm{g}^{0.25}}\right] \tag{17}$$

where, u_{am} is the average velocity of the mixed fluid, m/s; ρ_{am} is the average density of the mixed fluid, kg/m^3; D_e is the equivalent diameter, m; n is the flow index of the mixed fluids; f is the friction coefficient; ε_e is the equivalent absolute roughness; k is the correction factor; Re is the mean Reynolds number of the mixed fluids.

2.2.2 Fluid physical property calculation

Peng and Robinson equation of state (PR-EOS) [19] is used to calculate the gas phase compressibility factor. The basic form is as follows:

$$Z^3 - (1\text{-}B)\ Z^2 + (A\text{-}2B\text{-}3B^2)Z - (AB - B^2 - B^3) = 0 \tag{18}$$

$$A = \frac{aP}{(RT)^2} \tag{19}$$

$$B = \frac{bP}{RT} \tag{20}$$

where, R is the general gas constant, 8.314 J / (mol·K); P is the corresponding pressure, MPa; T is temperature, K; a and b are the parameters of gas gravity term and volume term in Peng and Robinson equation of state:

$$b = 0.0778\frac{RT_c}{P_c} \tag{21}$$

$$a = a(T_c)\alpha(T) \tag{22}$$

$$a(T_c) = 0.45724\frac{(RT_c)^2}{P_c} \tag{23}$$

$$\alpha(T) = \left[1+\beta\left(1-\sqrt{\frac{T}{T_c}}\right)\right]^2 \tag{24}$$

$$\beta = 0.37464 + 1.54226\omega - 0.26992\omega^2 \tag{25}$$

where, P_c, T_c and ω are the critical pressure of component i in the gas, MPa, Critical temperature, K, and Eccentricity factor.

Gas density is calculated by the following equation:

$$\rho_g = \frac{M_g P}{RTZ} \tag{26}$$

For the viscosity calculation of natural gas containing CO_2 and H_2S, the viscosity calculation formula of sour natural gas in Carr et al. [20] is adopted. See Appendix A. Considering that the dissolution effect of gas requires accurate gas dissolution, the solubility prediction model will be discussed and relevant gas water solubility experiments will be carried out. Velocity equation, two-phase flow pattern discrimination equation, and other auxiliary equations refer to Gao et al. (2007) [21].

2.2.3 Solubility calculation equation

The auxiliary equations of the model include friction pressure loss equation, section gas holdup equation, gas density equation and gas solubility equation [15, 16, 17]. This section mainly focuses on the analysis of gas solubility equation.

When the gas-liquid two phases reach equilibrium, the fugacity coefficients of the two phases are equal, that is:

$$f_i^g = f_i^l \tag{27}$$

where, f_i^g is the fugacity of the gas in the gas phase, i.e.:

$$f_i^g = p\phi_i y_i \tag{28}$$

For the calculation of fugacity of gas in liquid phase, the following formula is used:

$$f_i^l = h_i \gamma_i x_i \tag{29}$$

where, ϕ_i represents the fugacity coefficient of gas phase i in gas phase, γ_i is the activity coefficient of gas phase i in liquid phase, x_i is the mole fraction of gas phase i component in liquid phase, and y_i is the mole fraction of gas phase i component in gas-liquid equilibrium.

Therefore, the expression of gas mole fraction can be written as:

$$x_i = \frac{p\phi_i y_i}{h_i \gamma_i} \tag{30}$$

Here, Peng and Robinson equation of state (PR-EOS), Soave Redlich Kwong equation of state (SRK-EOS) and Redlich and Kwong equation of state (RK-EOS) [19, 22, 23] are selected for the calculation of gas fugacity coefficient, and the expression of fugacity coefficient is as follows

$$\text{PR:}\quad \ln\phi_i = \frac{b_i}{b}\left(\frac{PV}{RT}-1\right) - \ln\frac{P(V-b)}{RT} - \frac{a}{2\sqrt{2}bRT}\left(\frac{2\sum_{i=1}^{N} x_j a_{ij}}{a} - \frac{b_i}{b}\right)\ln\left(\frac{V+\left(\sqrt{2}+1\right)b}{V-\left(\sqrt{2}-1\right)b}\right) \tag{31}$$

$$\text{RK:}\quad \ln\phi_i = \frac{b_i}{b}\left(\frac{PV}{RT}-1\right) - \ln\frac{P(V-b)}{RT} + \frac{a}{bRT^{1.5}}\left(\frac{b_i}{b} - \frac{2\sum_{i=1}^{N} x_j a_{ij}}{a}\right)\ln\left(1+\frac{b}{V}\right) \tag{32}$$

$$\text{SRK:}\quad \ln\phi_i = \frac{b_i}{b}\left(\frac{PV}{RT}-1\right) - \ln\frac{P(V-b)}{RT} + \frac{a}{bRT}\left(\frac{b_i}{b} - \frac{2\sum_{i=1}^{N} x_j a_{ij}}{a}\right)\ln\left(1+\frac{b}{V}\right) \tag{33}$$

Where, b_i and b are the volume parameters of gas i and mixture respectively, dimensionless; a and a_{ij} are the gravitational term parameter of the mixture and the mixture of gas i and gas j, dimensionless; V is the molar volume of gas, m^3/mol; R is the general gas constant, J/(mol·K); P and T are the corresponding pressure, MPa and temperature, K; x_j is the mole fraction of gas j, dimensionless.

3 Model solution

3.1 Solution of solubility equation

For the calculation of gas solubility, the solution steps are as follows:

(1) Input the temperature and pressure, calculate the relevant parameters of each equation of state, and calculate the fugacity coefficient of gas components according to the calculated parameters of the equation of state;

(2) The Henry constant model proposed by Akinfiev and Diamond [24] is used to calculate the Henry constant of each gas component;

(3) The activity quotient of each gas component in aqueous solution or salt solution is calculated by using the activity coefficient calculation formula proposed by Duan et al. [11];

(4) The calculation results of (1) ~ (3) are substituted into Eq. (30) to obtain the content of gas components in the liquid phase.

3.2 Solution of multiphase flow model

The finite difference method is used for differential treatment of the multiphase flow model, which is not discussed here. The specific steps of the multiphase flow model are as follows:

(1) Estimate the bottom hole pressure $p_j^{n(0)}$ at time n and calculate the temperature T_j^n at time n.

(2) Calculate the solubility of j node gas in drilling fluid at time n. Judge according to the relationship between the calculated gas dissolution and formation gas production. If the calculated gas dissolution is less than the inflow production of gas, the gas dissolution at the current time is the calculated gas solubility. If the calculated gas dissolution is greater than the inflow production of gas, the gas dissolution at the current time is the inflow production of formation gas.

(3) According to the above calculated temperature and pressure at node j at time n, the production of each phase and the dissolution of gas flowing into the formation, the density, viscosity and other physical parameters of each component phase at node j at time n are calculated by using the Equation of state.

(4) The continuity equation is used to calculate the velocity and volume fraction of each component phase at j node at time n as the known parameters of j+1 spatial node at time n.

(5) Estimate the pressure p_{j+1}^n at j+1 node at time n, repeat steps (2) ~ (4), and calculate the $p_{j+1}^{n(0)}$ of j+1 node at time n from the momentum equation. If $\left|p_{j+1}^n - p_{j+1}^{n(0)}\right| \le \varepsilon$, the calculation is correct, take the calculated parameters of j + 1 node at time n as the known conditions of the next n+1 time, otherwise recalculate.

(6) Repeat (2) ~ (5) to the wellhead, and the calculated wellhead pressure is p_h. compared with the measured wellhead back pressure p_h^0. If $|p_h - p_h^0| < \varepsilon$ is true, the assumption of bottom hole pressure p_j^n at time n is correct. otherwise return to step (2) and reassign the bottom hole pressure $p_j^{n(0)}$ at time n.

4 Results and discussion

4.1 Optimization of solubility calculation models

For analyze the prediction accuracy of gas solubility model, the estimate consequences of solubility model of PR-EOS, SRK-EOS and RK-EOS are compared with the experimental data, expressed by Average Relative Deviation (*ARD%*) and Average Absolute Relative Deviation (*AARD%*):

$$ARD\% = \left(\frac{\left| x_{\exp} - x_{cal} \right|}{x_{\exp}} \right) \times 100 \tag{34}$$

$$AARD\% = \frac{1}{N_{\exp}} \sum \left(\frac{\left| x_{\exp} - x_{cal} \right|}{x_{\exp}} \right) \times 100 \tag{35}$$

Where, x_{exp} is the experimental data; x_{cal} is the predicted value of the model; $N_{\exp}$ is the number of experimental data points.

The experimental data used are the same as those listed in He et al. [25] literature and will not be repeated. Three EOS models are used to predict the experimental data, as shown in Fig 1. ~ Fig 3. Fig 1. shows the predicted distribution of ARD% of CH_4 water solubility experimental data by each equation of state. It can be seen from Fig 1. that the distribution density of ARD% calculated by PR-EOS and SRK-EOS is greater than that of RK-EOS in the low value area. The calculation results of AARD% show that the calculation accuracy of PR-EOS is higher, reaching 6.61 (as shown in Table 1). Fig 2 shows the calculated ARD%

distribution of the solubility prediction model on the experimental data of CO_2 water solubility. Compared with the prediction results of CH_4 gas, it is found that the distribution density of ARD% calculated by PR-EOS and RK-EOS in the low value region is greater than that of SRK-EOS. The predicted AARD% of PR-EOS, RK-EOS and SRK-EOS are 3.59, 4.76 and 10.05 respectively. Similarly, the solubility prediction calculation accuracy of PR-EOS is high. For the solubility prediction of $CO_2 + CH_4 + H_2S$ mixed gas solubility in water (as shown in Table 2), comparing the total solubility mole fraction of mixed gas with the prediction results (Fig 3), the prediction errors of the three models are large, but the ARD% value of PR-EOS is closer to 0. It is found that the AARD% calculation of each model has higher PR-EOS accuracy, which is 13.39. Therefore, the PR-EOS is selected to calculate the fugacity coefficient to calculate the solubility prediction.

Table 1. Calculation of experimental data by solubility prediction model under different equations of state AARD%.

Gas Type	AARD%		
	PR-EOS	RK-EOS	SRK-EOS
CH_4	6.61	8.18	12.68
CO_2	3.59	4.76	10.05
CH_4+CO_2+H_2S	13.39	15.44	15.804

Table 2. Experimental literature data of solubility of $CO_2 + CH_4 + H_2S$ in water.

Reference	T/K	P /MPa	Gas phase mole fraction			N_{exp}
			CO_2	H_2S	CH_4	
[26]	310-449	4.8-17.3	0.6	0.1	0.3	9
	380-449	7.5-18.1	0.1	0.8	0.1	5

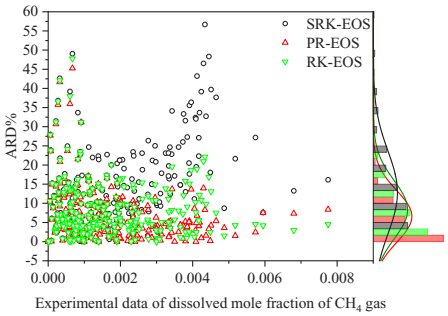

Fig. 1. Prediction of experimental data of CH_4 gas solubility by different EOS ARD%.

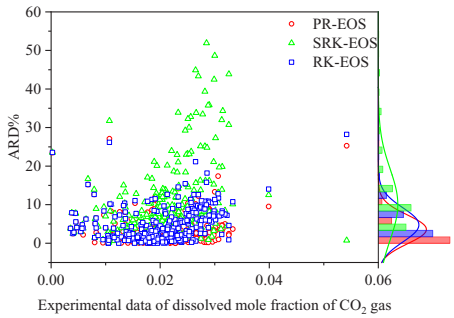

Fig. 2. Prediction of experimental data of CO_2 gas solubility by different EOS ARD%.

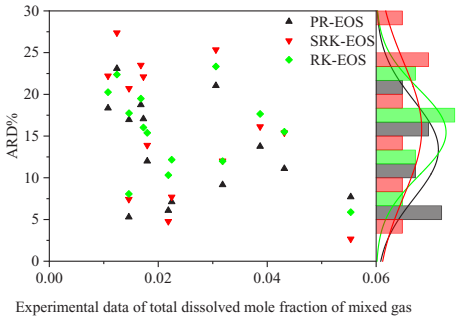

Fig. 3. Prediction of experimental data of CO_2+CH_4+H_2S gas solubility by different EOS.

4.2 Analysis of multiphase flow law

The basic parameters of the simulated deep well are listed in Table 3.

Table 3. Input data for the simulation.

Reservoir temperature /℃	62.6	Reservoir pressure /MPa	57.5
Permeability /md	10	Porosity	0.13
Temperature gradient / (℃·(100m)$^{-1}$)	2.8	Compressibility/(1·MPa^{-1})	2.0E-4
Water depth /m	1500	Well depth /m	4500
Gas invasion point /m	3300	Measure depth/m	3632.3
Mud density/(kg·m^{-3})	1500	Displacement/(L·s^{-1})	30
Surface temperature/℃	15	Mud viscosity/cP	30
Gas invasion time/s	5000	Drilling rate/ (m·h^{-1})	10
Gas type	97.5%CH_4+1.5%CO_2+1%H_2S		

Fig 4. displays the variation of solubility with well depth in different gas invasion time. With the increase of invasion time, the amount of gas in the invaded wellbore gradually increases, so that more gas is dissolved in the drilling fluid, resulting in the increase of solubility with the increase of invasion time. The gas solubility becomes 0. The closer the position is to the wellhead, the more blowout is likely to occur. Fig 5. indicates the relationship between bottom hole pressure and mud pit increment with invasion time when gas invasion occurs. The increase of invasion time leads to the increase of gas invasion, resulting in the decrease of liquid holdup in the annulus and the gradual decrease of bottom hole pressure. The increase of mud pit increment in water-based drilling fluid shows an exponential form. The mud pit increment has no obvious change with time at 0-500s, and the mud pit increment rises sharply with time after 500s. Within 0-500s, the gas dissolves into the drilling fluid. As time goes on, the dissolved gas gradually precipitates, and the volume of free gas increases, resulting in the increase of mud pit increment. According to the variation relationship of bottom hole pressure with time, with the increase of invasion time, the bottom hole pressure gradually decreases, resulting in the gradual increase of pressure difference between bottom hole and formation, the increase of invaded gas, and the further increase of mud pit increment.

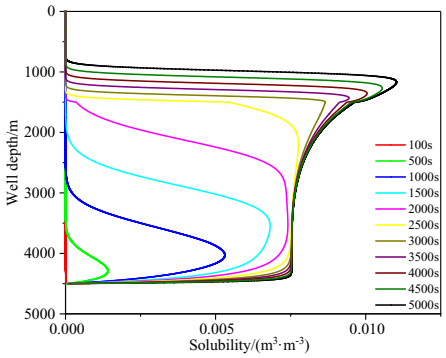

Fig. 4. Variation of solubility with well depth under different invasion time.

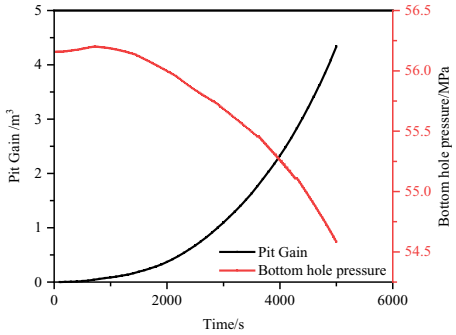

Fig. 5. Relationship between mud pit increment and bottom hole pressure with invasion time.

4.3 Analysis of influencing factors

Considering that there are many factors affecting the multiphase flow law in the drilling gas invasion stage, the effects of different gas types, drilling fluid displacement and permeability on the multiphase flow law are analyzed here. The specific example data are shown in Table 4.

Table 4. Case 1-3 basic calculation parameters.

	Permeability/md	**Gas invasion time/s**	**Drilling rate/ ($m \cdot h^{-1}$)**	**Displacement /($L \cdot s^{-1}$)**
Case1	10	4000	10	30
Case2	10	2500	10	10-35
Case3	0.1-100	2500	10	30

4.3.1 Case1: Sensitivity analysis of different gas types

Fig 6. Shows the variation of gas phase volume fraction with well depth under different CO_2 content. The lower the CO_2 content in the invaded gas, the greater the gas phase volume fraction at the bottom of the well. The main reason is that when the content of CO_2 in the invaded gas is very low, the dissolved amount of the invaded gas in the drilling fluid is very small, resulting in the increase of free gas. When the CO_2 content increases, because the solubility of CO_2 is peachier than that of CH_4 gas, the content of free gas is mainly CH_4. However, due to the low content of CH_4, the integral number of free gas is low.

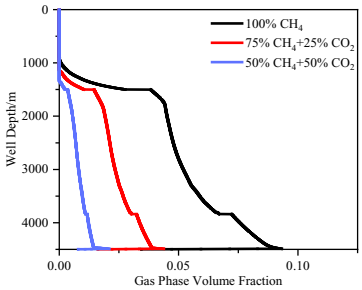

Fig. 6. The relationship between gas phase volume fraction and well depth.

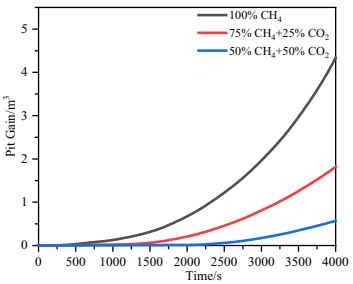

Fig. 7. Variation of mud pit gain with time under different CO_2 contents.

Fig 7. Shows the variation of mud pit increment with invasion time under different CO_2 content. When the CO_2 content decreases, the time to monitor the incremental change of mud pit is shorter. For example, when CO_2 free gas invasion, the increment of mud pit begins to rise at 500s, and the increment of 25% CO_2 begins to increase at 1300s. Therefore, the increase of CO_2 content in the invaded gas makes the monitoring of water-based drilling fluid more "hidden" in the initial stage of gas invasion. It takes longer to find gas invasion, which is more likely to cause blowout accidents.

Fig 8. Shows the influence of 50% CO_2 + 50% CH_4 gas invasion with and without gas dissolution on mud pit increment in case of gas invasion. When gas dissolution is not considered, the mud pit increment begins to increase at 250s, which is easier to detect on the platform. Considering the gas dissolution, the gas was completely dissolved in the drilling fluid in the early stage, and there was no obvious change in the mud pit increment from 0 to 2000s. It began to rise sharply after 2000s. It was found that the gas invasion time was later, resulting in the increase of "concealment" of gas invasion.

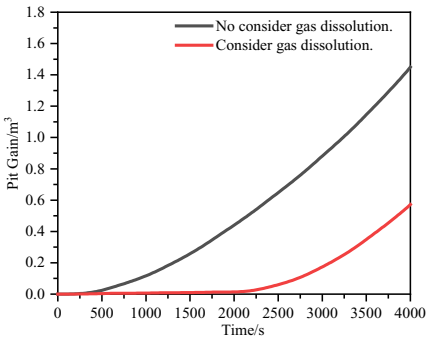

Fig. 8. Considering 50 % CO_2 + 50 % CH_4 gas dissolution and without considering the relationship between the increment of dissolved mud pool and time.

4.3.2 Case2: Sensitivity analysis of different drilling fluid displacement

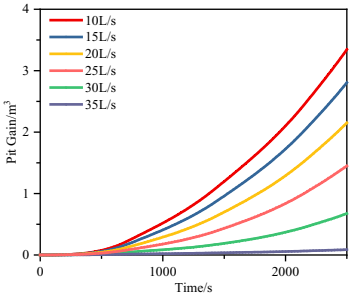

Fig. 9. Variation of mud pit increase with invasion time.

Fig 9. shows the variation of mud pit increment with gas invasion time under different drilling fluid displacement. With the increase of drilling fluid displacement, the mud pit increment decreases gradually. At low displacement, the amount of invaded gas is large, the ability of drilling fluid to dissolve gas is very low, and the volume of free gas in the annulus is very large. When reaching the drilling platform, the increment of mud pit is increased due to the high free gas content in the annulus. Fig 10. shows the change of gas volume fraction under different drilling fluid displacement when gas invasion occurs. The increase of drilling fluid displacement increases the bottom hole pressure, which reduces the pressure difference between formation and bottom hole, reduces the amount of invaded gas, and further reduces the gas content due to the dissolution of gas.

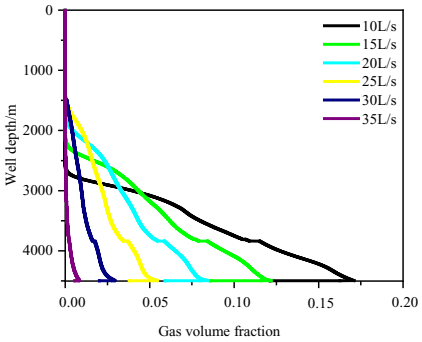

Fig. 10. Gas volume fraction at different depth relationship when the displacement gas invasion.

4.3.3 Case3: Sensitivity analysis of different permeability

Fig 11. shows the variation relationship of mud pit increment with invasion time under different permeability. With the increase of permeability, the mud pit increment gradually increases. The amount of gas invaded under high permeability is large, and the ability of drilling fluid to dissolve gas is limited, so there is more free gas, which makes the mud pit increment change more obvious under high permeability. Compared with low permeability, the gas influx is small and the dissolution is significant, so that the increment change of mud pit is basically 0.

Fig 12. shows the variation of gas phase volume fraction with well depth under different permeability. With the increase of permeability, the amount of gas invading the annulus increases and the amount of gas dissolved in the drilling fluid increases. However, the solubility in the drilling fluid is limited and the amount of dissolution is much smaller than

the amount of invasion. Therefore, the gas phase volume fraction under high permeability is large.

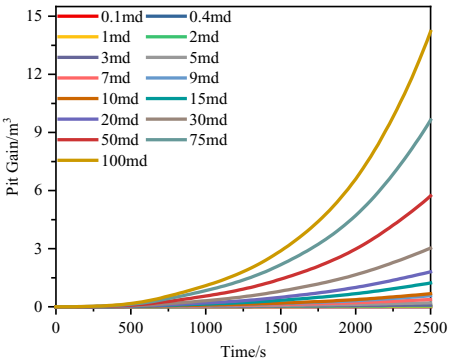

Fig. 11. Variation of mud pool increment with time at different permeability.

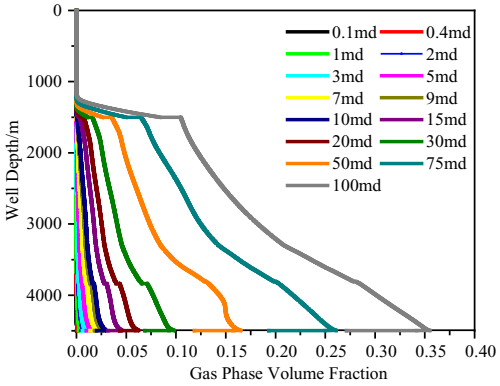

Fig. 12. Relationship between gas volume fraction and depth of well under different permeability.

5 Conclusion

By solving the multiphase flow model considering dissolution after the invasion of high CO_2 gas and optimizing the gas solubility prediction model, the following conclusions are obtained:

(1) The solubility prediction of fugacity coefficient calculated by different state equations shows that the PR-EOS has higher prediction accuracy for the solubility of CH_4, CO_2 and $CH_4 + CO_2 + H_2S$ in water, which is better than the solubility models of SRK-EOS and RK-EOS.

(2) According to the analysis of multiphase flow law, for different gas invasion duration, the solubility of gas in drilling fluid shows the trend of "gradually increasing and rapidly decreasing when reaching the wellhead" from the bottom of the well to the wellhead. The closer the initial precipitation position of dissolved gas is to the wellhead, the higher the "concealment" of gas invasion.

(3) Compared with ignoring the dissolution of gas in drilling fluid, considering the dissolution of gas, the increment of mud pit increases more slowly, and the time to reach the gas invasion alarm value increases greatly. The higher the CO_2 content in the intrusive gas, the greater the solubility of the intrusive gas in the drilling fluid and the decrease of the gas phase volume fraction in the drilling fluid, resulting in the insignificant change of gas

invasion monitoring parameters such as mud pit increment, and finally the gas invasion is difficult to be found in time.

This paper is supported by the National Natural Science Foundation of China (U1762216), Postdoctoral innovative talents support program in Shandong Province (SDBX2020005).

References

1. J. Zhao, Natural Gas Industry, 27-2, (2007) 141-144.
2. Z. Zhi, F. Hong, H. T. Shi, Society of Petroleum Engineers, (2010).
3. N. Moroni, C. Repetto, K. Ravi, Society of Petroleum Engineers, (2008).
4. G. Verri, K. S. Sorbie, M. A. Singleton, SPE International Oilfield Scale Conference and Exhibition, 2016.
5. L. K. Wang, G. J. Chen, G. H. Han, Fluid Phase Equilibria, 207-1, (2003) 143-154.
6. O. L. Culberson, J. J. McKetta, Petrol. Technol, 2-11, (1950) 319-322.
7. O. L. Culberson, J. J. Mcketta, Trans. Am. Inst. Min. Met. Eng. 192-1, (1951) 223-226.
8. C. W. Blount, L. C. Price, Final Report (1982).
9. I. Søreide, C. H. Whitson, Fluid Phase Equilib. 77, (1992) 217-240.
10. J. J. Carroll, A. E. Mather, Chemical Engineering Science, 52, (1997) 545-552.
11. Z. Duan, S. Mao, Geochimica Et Cosmochimica Acta, 70, (2006) 3369-3386.
12. M. Zirrahi, R. Azin, H. Hassanzadeh, Fluid Phase Equilibria, 32, (2012) 80-93.
13. Z. Ziabakhsh-Ganji, H. Kooi, International Journal of Greenhouse Gas Control, 11, (2012) 21-34.
14. J. Li, L. Wei, X. Li, Energy Procedia, 63, (2014) 3598-3607.
15. B. Sun, W. Fu, N. Wang, Journal of Petroleum Science and Engineering, 174, (2019) 1142-1151.
16. Z. Xu, X. Song, G. Li, Applied Thermal Engineering, 149, (2018) 1080-1097.
17. B. Yin, G. Liu, X. Li, Applied Mathematical Modelling, 51, (2017) 159-198.
18. B. Sun, P. Gong, Z. Wang, J. Hydrodyn. Ser. B 25 (2) (2013) 264-273.
19. D. Y. Peng, D. B. Robinson, Industrial and Engineering Chemistry Research, 15, (1976) 59-64.
20. N. L. Carr, R. Kobayashi, D. B. Burrows, Journal of Petroleum Technology, 6(10), (1954) 47-55.
21. G. Yonghai, Doctoral dissertation. China University of Petroleum, 2007. 47-64.
22. O. Redlich, J. Kwong, Chemical Reviews, 44, (1949) 233.
23. G. Soave, Chem. Eng. Sci, 27, (1972) 1197-1203.
24. N. N. Akinfiev, L. W. Diamond, Geochim.Et. Cosmochim. Acta 67, (2003) 613-629.
25. H. He, B. Sun, Z. Wang, Journal of Petroleum Science and Engineering, 192, (2020) 107337.
26. S. S. Huang, A. D. Leu, H. J. Ng, Fluid Phase Equilibria, 19, (1985) 21-32.